Mon. Not. R. Astron. Soc. **307**, 433–448 (1999)

The kinematics and the origin of the ionized gas in NGC 4036

P. Cinzano,[1★] H.-W. Rix,[2,3] M. Sarzi,[1] E. M. Corsini,[4] W. W. Zeilinger[5] and F. Bertola[1]

[1]*Dipartimento di Astronomia, Università di Padova, vicolo dell'Osservatorio 5, I-35122 Padova, Italy*
[2]*Max Planck Institut für Astrophysik, Karl Schwarzschild Straße 1, D-85748 Garching bei München, Germany*
[3]*Steward Observatory, University of Arizona, Tucson, AZ-85721, USA*
[4]*Osservatorio Astrofisico di Asiago, Dipartimento di Astronomia, Università di Padova, via dell'Osservatorio 8, I-36012 Asiago, Italy*
[5]*Institut für Astronomie, Universität Wien, Türkenschanzstraße 17, A-1180 Wien, Austria*

Accepted 1999 March 2. Received 1998 November 6; in original form 1995 July 10

ABSTRACT

We present the kinematics and photometry of the stars and of the ionized gas near the centre of the S0 galaxy NGC 4036. Dynamical models based on the Jeans equation have been constructed from the stellar data to determine the gravitational potential in which the ionized gas is expected to orbit. Inside 10 arcsec, the observed gas rotation curve falls well short of the predicted circular velocity. Over a comparable radial region the observed gas velocity dispersion is far higher than that expected from thermal motions or small-scale turbulence, corroborating that the gas cannot be following the streamlines of nearly closed orbits. We explore several avenues to understand the dynamical state of the gas. (1) We treat the gas as a collisionless ensemble of cloudlets and apply the Jeans equation to it; this modelling shows that inside 4 arcsec the gas velocity dispersion is just high enough to explain quantitatively the absence of rotation. (2) Alternatively, we explore whether the gas may arise from the 'just shed' mass-loss envelopes of the bulge stars, in which case their kinematics should simply mimic that of the stars; the latter approach matches the data better than (1), but still fails to explain the low velocity dispersion *and* slow rotation velocity of the gas for $5 < r < 10$ arcsec. (3) Finally, we explore whether drag forces on the ionized gas may aid in explaining its peculiar kinematics. While all these approaches provide a much better description of the data than cold gas on closed orbits, we do not yet have a definitive model to describe the observed gas kinematics at all radii. We outline observational tests to understand the enigmatic nature of the ionized gas.

Key words: galaxies: elliptical and lenticular, cD – galaxies: individual: NGC 4036 – galaxies: ISM – galaxies: kinematics and dynamics – galaxies: structure.

1 INTRODUCTION

Stars and ionized gas provide independent probes of the mass distribution in a galaxy. The comparison between their kinematics is particularly important in dynamically hot systems (i.e., whose projected velocity dispersion is comparable to rotation). In fact, in elliptical galaxies and bulges the ambiguities about orbital anisotropies can lead to considerable uncertainties in the mass modelling (e.g. Binney & Mamon 1982; Rix et al. 1997).

The mass distributions inferred from stellar and gaseous kinematics are usually in good agreement for discs (where both tracers can be considered on nearly circular orbits), but often appear discrepant for bulges (e.g. Fillmore, Boroson & Dressler 1986; Kent 1988; Kormendy & Westpfahl 1989; Bertola et al. 1995b). There are several possibilities to explain these discrepant mass estimates in galactic bulges.

(i) If bulges have a certain degree of triaxiality, depending on the viewing angle the gas on closed orbits can either move faster or slower than in the 'corresponding' axisymmetric case (Bertola, Rubin & Zeilinger 1989). Similarly, the predictions of the triaxial stellar models deviate from those in the axisymmetric case: whenever $\sigma_{\rm stars} > \sigma_{\rm axisym}$, then $v_{\rm stars} < v_{\rm axisym}$.

(ii) Most of the previous modelling assumes that the gas is dynamically cold and therefore rotates at the local circular speed on the galactic equatorial plane. If in bulges the gas velocity dispersion $\sigma_{\rm gas}$ is not negligible (e.g. Cinzano & van der Marel 1994, hereafter CvdM94; Bertola et al. 1995b; Rix 1995), the gas rotates more slowly than the local circular velocity due to its dynamical pressure support. CvdM94 showed explicitly for the E4/S0a galaxy NGC 2974 that the gas and star kinematics agree,

★ E-mail: cinzano@pd.astro.it

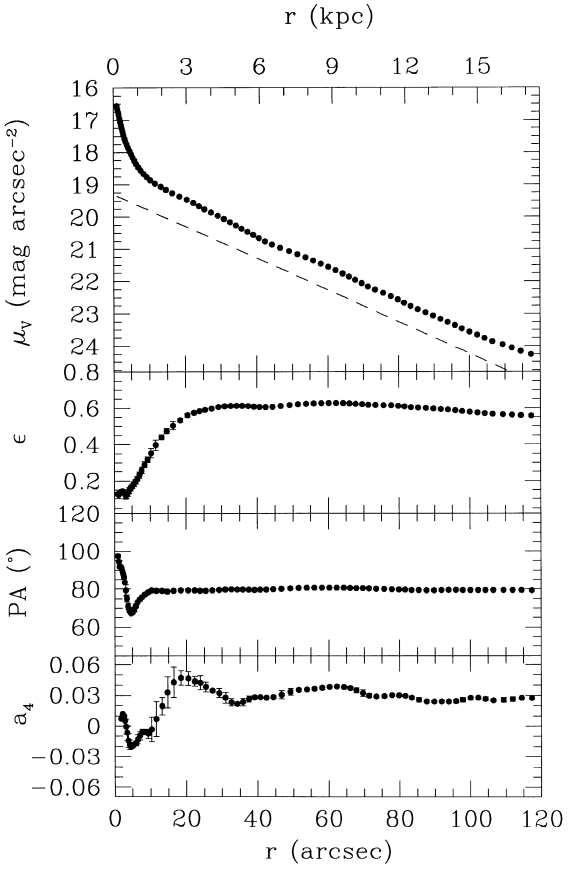

Figure 1. Ground-based *V*-band observed surface-brightness, ellipticity, position angle and $\cos 4\theta$ coefficient radial profiles of NGC 4036. The dashed line in the top panel represents the surface-brightness profile of the exponential disc of the best-fitting kinematical model ($\mu_0 = 19.3$ mag arcsec^{-2}, $r_d = 22.0$ arcsec and $i = 72°$) derived in Section 3.2.3.

taking into account the gas velocity dispersion. Furthermore, if σ_{gas} is comparable to the observed streaming velocity, the spatial gas distribution can no longer be modelled as a disc.

(iii) Forces other than gravity (such as magnetic fields, interactions with stellar mass-loss envelopes and the hot gas component) might act on the ionized gas (e.g. Mathews 1990).

In this paper we pursue the second of these explanations by building for NGC 4036 dynamical models which take into account both the random motions and the three-dimensional spatial distribution of the ionized gas.

NGC 4036 has been classified $S0_3(8)$/Sa in RSA (Sandage & Tammann 1981) and $S0^-$ in RC3 (de Vaucouleurs et al. 1991). It is a member of the LGG 266 group, together with NGC 4041, IC 758, UGC 7009 and UGC 7019 (Garcia 1993). It forms a wide pair with NGC 4041, with a separation of 17 arcmin corresponding to 143 kpc at their mean redshift distance of 29 Mpc (Sandage & Bedke 1994). In The Carnegie Atlas of Galaxies (hereafter CAG) Sandage & Bedke describe it as characterized by an irregular pattern of dust lanes threaded through the disc in an 'embryonic' spiral pattern indicating a mixed S0/Sa form (see panel 60 in CAG). Its total *V*-band apparent magnitude is $V_T = 10.66$ mag (RC3). This corresponds to a total luminosity $L_V = 4.2 \times 10^{10}\,L_{\odot V}$ at the assumed distance of $d = 30.2$ Mpc. The distance of NGC 4036 was derived as $d = V_0/H_0$ from the systemic velocity corrected for the motion of the Sun with respect to the centroid of the Local Group $V_0 = 1509 \pm 50$ km s^{-1} (RSA) and assuming $H_0 = 50$ km s^{-1} Mpc^{-1}. At this distance the scale is 146 pc arcsec^{-1}.

The total masses of neutral hydrogen and dust in NGC 4036 are $M_{HI} = 1.7 \times 10^9\,M_\odot$ and $M_{dust} = 4.4 \times 10^5\,M_\odot$ (Roberts et al. 1991). NGC 4036 is known to have emission lines from ionized gas (Bettoni & Buson 1987), and the mass of the ionized gas is $M_{HII} = 7 \times 10^4\,M_\odot$ (see Section 4.1 for a discussion).

This paper is organized as follows. In Section 2 we present the photometric and spectroscopic observations of NGC 4036, the reduction of the data, and the analysis procedures to measure the surface photometry and the major-axis kinematics of stars and ionized gas. In Section 3 we describe the stellar dynamical model (based on the Jeans equations), and we find the potential due to the stellar bulge and disc components starting from the observed surface brightness of the galaxy. In Section 4 we use the derived potential to study the dynamics of both the gaseous spheroid and disc components, assumed to be composed of collisionless cloudlets orbiting as test particles. In Section 5 we discuss our conclusions.

2 OBSERVATIONS AND DATA ANALYSIS

2.1 Photometric observations

2.1.1 Ground-based data

We obtained an image of NGC 4036 of 300-s exposure in the Johnson *V* band at the 2.3-m Bok Telescope at the Kitt Peak National Observatory on 1995 December 22.

A front-illuminated 2048×2048 LICK2 Loral CCD with $15 \times 15\,\mu m^2$ pixels was used as detector at the Richtey–Chretien focus, *f*/9. It yielded a flat field of view with a 10.1 arcmin diameter. The image scale was 0.43 arcsec pixel^{-1} after a 3×3 pixel binning. The gain and the readout noise were 1.8 e$^-$ ADU^{-1} and 8 e$^-$ respectively.

The data reduction was carried out using standard IRAF[1] routines. The image was bias-subtracted and then flat-field-corrected. The cosmic rays were identified and removed. A Gaussian fit to field stars in the resulting image yielded a measurement of the seeing point spread function (PSF) FWHM of 1.7 arcsec.

The sky subtraction and elliptical fitting of the galaxy isophotes were performed by means of the Astronomical Images Analysis Package (AIAP) developed at the Osservatorio Astronomico di Padova (Fasano 1990). The sky level was determined by a polynomial fit to the surface brightness of the frame regions not contaminated by the galaxy light, and then subtracted out from the total signal. The isophote fitting was performed by masking the bad columns of the frame and the bright stars of the field. Particular care was taken in masking the dust-affected regions along the major axis between 5 and 20 arcsec. No photometric standard stars were observed during the night. For this reason the absolute calibration was made by scaling the total apparent *V*-band magnitude to $V_T = 10.66$ mag (RC3).

Fig. 1 shows the *V*-band surface brightness (μ_V), ellipticity (ϵ), major axis position angle (PA), and the $\cos 4\theta$ (a_4) Fourier

[1] IRAF is distributed by the National Optical Astronomy Observatories, which are operated by the Association of Universities for Research in Astronomy (AURA) under cooperative agreement with the National Science Foundation.

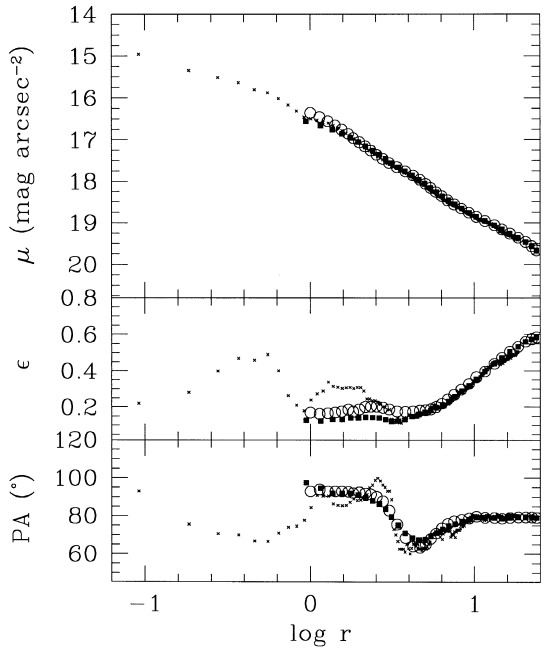

Figure 2. Surface-brightness, ellipticity and position angle radial profiles of the nuclear regions of NGC 4036 obtained from a *HST* image (crosses) compared to the ground-based data before (filled squares) and after (open circles) the seeing-deconvolution (see Section 3.2.1). The WFPC image is in the F547W band, while the ground-based images are in the *V* band.

coefficient of the isophote's deviations from elliptical as functions of radius along the major axis.

For $r \lesssim 4$ arcsec the ellipticity is $\gtrsim 0.12$. Between $r \sim 4$ and ~ 30 arcsec it increases to 0.61. It rises to 0.63 at $r \sim 62$ arcsec, and then it decreases to 0.56 at the farthest observed radius. The position angle ranges from $\sim 98°$ to $\sim 67°$ in the inner 5 arcsec. Between $r \sim 5$ and ~ 10 arcsec it increases to $\sim 79°$, and then it remains constant. The $\cos 4\theta$ coefficient ranges between $\sim +0.01$ and ~ -0.02 for $r \lesssim 5$ arcsec. Further out it peaks to $\sim +0.05$ at $r \sim 18$ arcsec, and then it decreases to $\sim +0.03$ for $r > 30$ arcsec. The abrupt variation in position angle ($\Delta PA \simeq 30°$) observed inside 5 arcsec leads to an isophote twist that can be interpreted as due to a slight triaxiality of the inner regions of the stellar bulge. Anyway this variation has to be considered carefully due to the presence of dust pattern in these regions which are revealed by *HST* imaging (see Fig. 2).

These results are consistent with previous photometric studies of Kent (1984) and Michard (1993), obtained in the *r* and *B* bands respectively. Our measurements of ellipticity follow closely those by Michard. Kent (1984) measured the ellipticity and position angle of NGC 4036 isophotes in the *r*-band for $9 \leq r \leq 114$ arcsec. Out to $r = 78$ arcsec the *r*-band ellipticity is lower than our *V*-band one by ~ 0.04. The *r*-band position angle profile differs from ours only at $r \sim 16$ arcsec ($\epsilon_r = 76°$) and for $r > 78$ arcsec ($\epsilon_r = 81°$). We found the $\cos 4\theta$ isophote deviation from ellipses to have a radial profile in agreement with that by Michard.

2.1.2 *Hubble Space Telescope data*

In addition, we derived the ionized gas distribution in the nuclear regions of NGC 4036 by the analysis of two Wide Field Planetary Camera 2 (WFPC2) images which were extracted from the *Hubble Space Telescope* (*HST*) archive.[2]

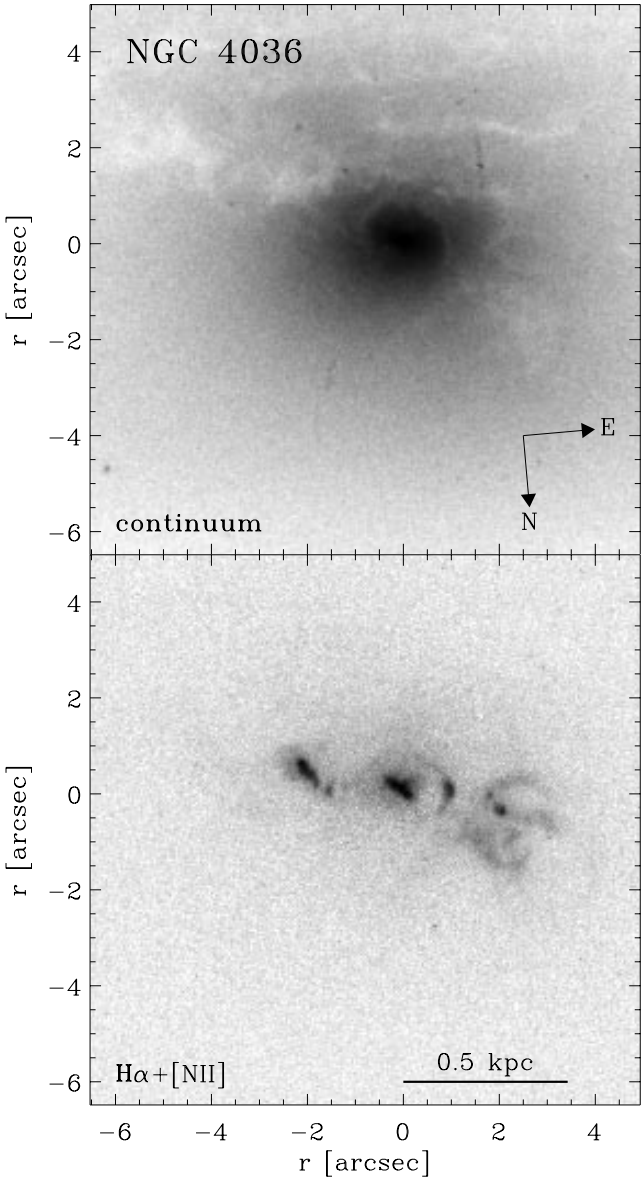

Figure 3. WFPC2 stellar continuum image (upper panel) and the continuum-subtracted Hα+[N II] emission image (lower panel) of the nucleus of NGC 4036.

We used a 300-s image obtained on 1994 August 08, with the F547M filter (principal investigator: Sargent GO-05419), and a 700-s image taken on 1997 May 15, with the F658N filter (principal investigator: Malkan GO-06785).

The standard reduction and calibration of the images were performed at the STScI using the pipeline-WFPC2 specific calibration algorithms. Further processing using the IRAF STSDAS package involved the cosmic rays removal and the alignment of the images (which were taken with different position angles). The surface photometry of the F547M image was carried out using the STSDAS task ELLIPSE without masking the dust lanes. In Fig. 2 we

[2] Observations with the NASA/ESA *Hubble Space Telescope* were obtained from the data archive at the Space Telescope Science Institute (STScI), operated by AURA under NASA contract NAS 5-26555.

plot the resulting ellipticity (ϵ) and major axis position angle (PA) of the isophotes as functions of radius along the major axis.

The continuum-free image of NGC 4036 (Fig. 3) was obtained by subtracting the continuum-band F547M image, suitably scaled, from the emission-band F658N image. The mean scalefactor for the continuum image was estimated by comparing the intensity of a number of 5×5 pixels regions near the edges of the frames in the two bandpasses. These regions were chosen in the F658N image to be emission-free. Our continuum-free image reveals that less than the 40 per cent of the Hα + [N II] flux of NGC 4036 derives from a clumpy structure of about 6×2 arcsec^2. The centre of this complex filamentary structure, which is embedded in a smooth emission pattern, coincides with the position of the maximum intensity of the continuum.

2.2 Spectroscopic observations

A major-axis (PA = 85°) spectrum of NGC 4036 was obtained on 1989 March 30, with the Red Channel Spectrograph at the Multiple Mirror Telescope[3] as a part of a larger sample of eight S0 galaxies (Bertola et al. 1995b).

The exposure time was 3600 s, and the 1200 groove mm^{-1} grating was used in combination with a 1.25×180 arcsec^2 slit. This yielded a wavelength coverage of 550 Å between about 3650 Å and about 4300 Å, with a reciprocal dispersion of 54.67 Å mm^{-1}. The spectral range includes stellar absorption features, such as the the Ca II H and K lines ($\lambda\lambda$3933.7, 3968.5 Å) and the Ca I g-band (λ4226.7 Å), and the ionized gas [O II] emission doublet ($\lambda\lambda$3726.2. 3728.9 Å). The instrumental resolution was derived measuring the σ of a sample of single emission lines distributed over all the spectral range of a comparison spectrum after calibration. We checked that the measured σs did not depend on wavelength, and we found a mean value $\sigma = 1.1$ Å. This corresponds to a velocity resolution of ~ 88 km s^{-1} at 3727 Å, and ~ 83 km s^{-1} at 3975 Å. The adopted detector was the 800×800 Texas Instruments CCD, which has a 15×15 μm^2 pixel size. No binning or rebinning was done. Therefore each pixel of the frame corresponds to 0.82 Å $\times 0.33$ arcsec.

Some spectra of late-G and early-K giant stars were taken with the same instrumental set-up for use as velocity and velocity dispersion templates in measuring the stellar kinematics. Comparison helium-argon lamp exposures were taken before and after every object integration. The seeing FWHM during the observing night was between 1 and 1.5 arcsec.

The data reduction was carried out with standard procedures from the ESO MIDAS[4] package. The spectra were bias-subtracted, flat-field-corrected, cleaned for cosmic rays, and wavelength-calibrated. The sky contribution in the spectra was determined from the edges of the frames and then subtracted.

2.2.1 *Stellar kinematics*

The stellar kinematics was analysed with the Fourier Quotient Method (Sargent, Schechter & Boksenberg 1977) as applied by Bertola et al. (1984). The K4III star HR 5201 was taken as template. It has a radial velocity of -2.7 km s^{-1} (Evans 1967) and a rotational velocity of 10 km s^{-1} (Bernacca & Perinotto 1970). No attempt was made to produce a master template by combining the spectra of different spectral types, as was done by Rix & White (1992) and van der Marel et al. (1994). The template spectrum was averaged along the spatial direction to increase the signal-to-noise ratio (*S/N*). The galaxy spectrum was rebinned along the spatial direction until a ratio $S/N \geq 10$ was achieved at each radius. Then spectra of galaxy and template star were rebinned to a logarithmic wavelength scale, continuum-subtracted and end-masked. The least-squares fitting of a Gaussian-broadened spectrum of the template star to the galaxy spectrum was done in the Fourier space over the restricted range of wavenumbers $[k_{\min}, k_{\max}] = [5, 200]$. In this way we rejected the low-frequency trends (corresponding to $k < 5$) due to the residuals of continuum subtraction and the high-frequency noise (corresponding to $k > 200$) due to the instrumental resolution. (The wavenumber range is important, particularly in the Fourier fitting of lines with non-Gaussian profiles; see van der Marel & Franx 1993 and CvdM94.)

The values obtained for the stellar radial velocity and velocity dispersion as a function of radius are given in Table A1. This table reports the galactocentric distance r in arcsec (column 1), the heliocentric velocity V (column 2) and its error δV (column 3)

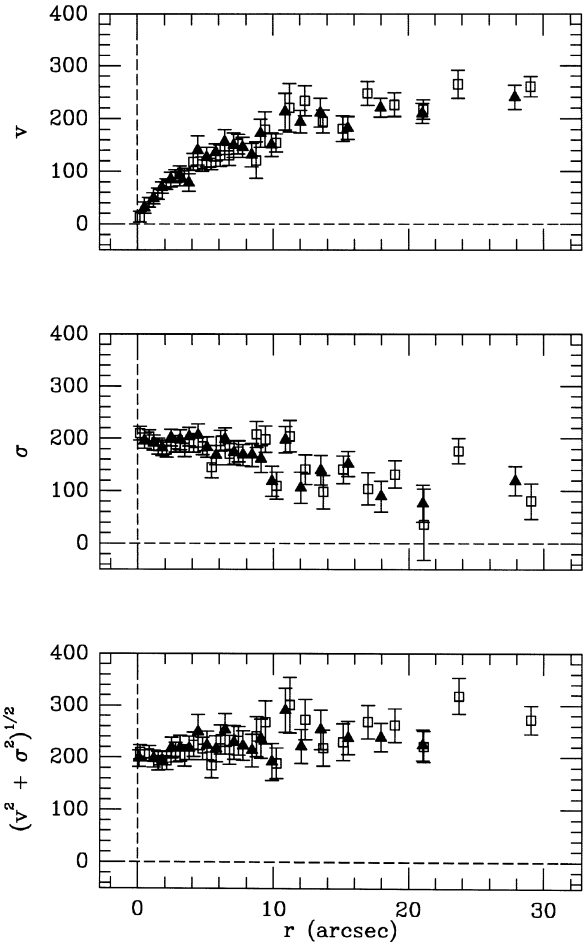

Figure 4. Stellar kinematics along the major axis of NGC 4036. The folded rotation velocity curve (top panel), velocity dispersion profile (middle panel) and rms velocity curve (bottom panel) are shown in km s^{-1}. Open squares and filled triangles represent data derived for the approaching west and receding east sides respectively.

[3] The MMT is a joint facility of the Smithsonian Institution and the University of Arizona.

[4] MIDAS is developed and mantained by the European Southern Observatory.

in km s^{-1}, and the velocity dispersion σ (column 4) and its error $\delta\sigma$ (column 5) in km s^{-1} . The values for the stellar δV and $\delta\sigma$ are the formal errors from the fit in the Fourier space.

The systemic velocity was subtracted from the observed heliocentric velocities, and the profiles were folded about the centre, before plotting. We derive for the systemic heliocentric velocity a value $V_\odot = 1420 \pm 15$ km s^{-1}. Our determination is in agreement within the errors with $V_\odot = 1397 \pm 27$ km s^{-1} (RC3) and $V_\odot = 1382 \pm 50$ km s^{-1} (RSA) also derived from optical observations. The resulting rotation curve, velocity dispersion profile and rms velocity ($\sqrt{v^2 + \sigma^2}$) curve for the stellar component of NGC 4036 are shown in Fig. 4. The kinematical profiles are symmetric within the error bars with respect to the galaxy centre. For $r \lesssim 2$ arcsec the rotation velocity increases almost linearly with radius up to ~ 100 km s^{-1}, remaining approximatively constant between 2 and 4 arcsec. Outwards it rises to the farthest observed radius. It is ~ 180 km s^{-1} at 9 arcsec, ~ 220 km s^{-1} at 21arcsec and ~ 260 km s^{-1} at 29 arcsec. The velocity dispersion $\sigma \sim 210$ km s^{-1} at the centre and at $r \sim 4$ arcsec, with a local minimum of ~ 180 at $r = 2$ arcsec. Further out it declines to values $\lesssim 120$ km s^{-1}.

2.2.2 *Ionized gas kinematics*

To determine the ionized gas kinematics, we studied the [O II] ($\lambda\lambda$3726.2, 3728.9 Å) emission doublet. In our spectrum the two lines are not resolved at any radius. We obtained smooth fits to the [O II] doublet using a two-step procedure. In the first step the emission doublet was analysed by fitting a double Gaussian to its line profile, fixing the ratio between the wavelengths of the two lines and assuming that both lines have the same dispersion. The intensity ratio of the two lines depends on the state (i.e., electron density and temperature) of the gas (e.g. Osterbrock 1989). We found a mean value of [O II]λ3726.2/[O II]λ3728.9 $= 0.8 \pm 0.1$, without any significant dependence on radius. The electron density derived from the obtained intensity ratio of [O II] lines is in agreement with that derived (at any assumed electron temperature; see Osterbrock 1989) from the intensity ratio of the [S II] lines ([S II] λ6716.5/[S II] λ6730.9 = 1.23) found by Ho, Filippenko & Sargent (1997). In the second step we fitted the line profile of the emission doublet by fixing the intensity ratio of its two lines at the value above. At each radius we derived the position, the dispersion and the uncalibrated intensity of each [O II] emission line and their formal errors from the best-fitting double Gaussian to the doublet plus a polynomial to its surrounding continuum. The wavelength of the line centre was converted into the radial velocity, and then the heliocentric correction was applied. The line dispersion was corrected for the instrumental dispersion and then converted into the velocity dispersion.

The measured kinematics for the gaseous component in NGC 4036 is given in Table A2. This table contains the galactocentric distance r in arcsec (column 1), the heliocentric velocity V (column 2) and its error δV (column 3) in km s^{-1}, and the velocity dispersion σ (column 4) and its errors $\delta\sigma_+$ and $\delta\sigma_-$ (columns 5 and 6) in km s^{-1} . The gas velocity errors δV are the formal errors for the double-Gaussian fit to the [O II] doublet. The gas velocity dispersion errors $\delta\sigma_+$ and $\delta\sigma_-$ also take account of the subtraction of the instrumental dispersion.

The rotation curve, velocity dispersion profile and rms velocity curve for the ionized gas component of NGC 4036 resulting after folding about the centre are shown Fig. 5. The [O II] λ3726.2

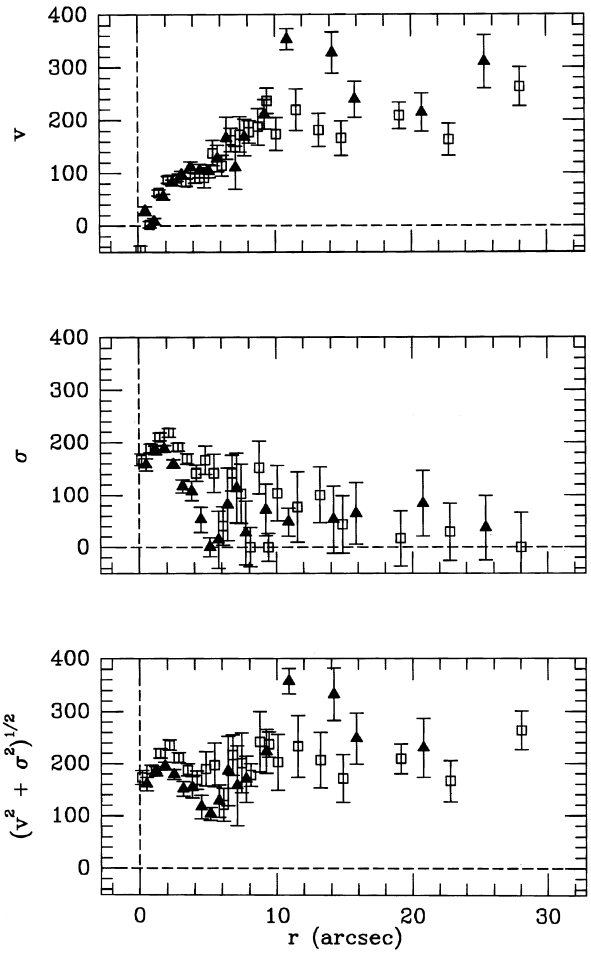

Figure 5. Ionized-gas kinematics along the major axis of NGC 4036. The folded rotation velocity curve (top panel), velocity dispersion profile (middle panel) and rms velocity curve (bottom panel) are shown in km s^{-1}. Open squares and filled triangles represent data derived for the approaching west and receding east sides respectively. The velocity error bars indicate the formal error of double Gaussian fit to the [O II] doublet. The error bars in the velocity dispersions also take into account the subtraction of the instrumental dispersion.

intensity profile as a function of radius is plotted in Fig. 6. The gas rotation tracks the stellar rotation remarkably well. They are consistent within the errors of one another. The gas velocity dispersion has central dip of ~ 160 km s^{-1}, with a maximum of $\sim$220 km s^{-1} at $r \sim 2$ arcsec. It remains higher than 100 km s^{-1} up to ~ 4 arcsec, before decreasing to lower values. The velocity dispersion profile appears to be less symmetric than the rotation curve. Indeed, between 2 and 5 arcsec the velocity dispersion measured on the east side drops rapidly from its observed maximum to ~ 50 km s^{-1}, while on the west side it declines smoothly to $\sim$140 km s^{-1}. Errors on the gas velocity dispersion increase at large radii, as the gas velocity dispersion becomes comparable to the instrumental dispersion.

2.2.3 *Comparison with kinematical data by Fisher (1997)*

The major-axis kinematics for stars and gas we derived for NGC 4036 are consistent within the errors with the measurements of Fisher (1997, hereafter F97). The only exception is represented by the differences of 20–30 per cent between our and F97 stellar

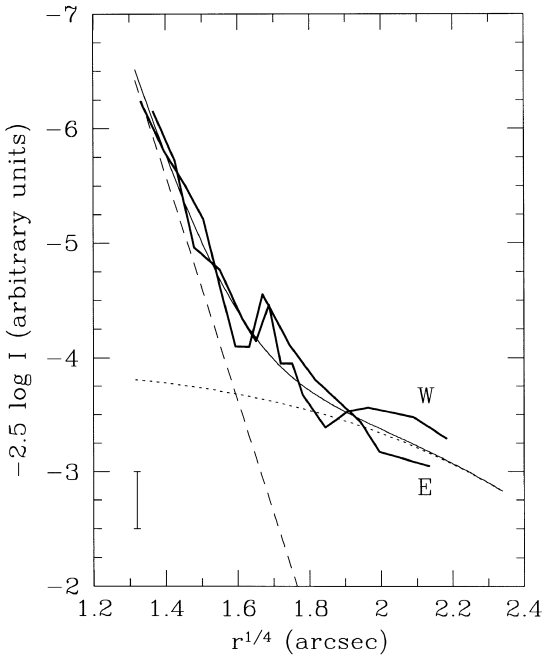

Figure 6. The intensity of the [O II]] λ3726.2 line as function of radius in NGC 4036. Since the spectrum was not flux-calibrated, the scale has an arbitrary zero-point. The thick continuous lines connect the measurements along the west and east sides respectively. The vertical bar on the left-hand side of the panel represents the typical error for the data. The dashed and dotted lines represent respectively the profile of the gaseous $R^{1/4}$ spheroid and gaseous exponential disc derived in Section 4.1. The thin continuous line is the fit to the data.

velocity dispersions in the central 8 arcsec. In these regions F97 finds a flat velocity dispersion profile with a plateau at $\sigma \sim 170\,\mathrm{km\,s^{-1}}$. To measure stellar kinematics, he adopted the Fourier Fitting Method (van der Marel & Franx 1993) directly on the line-of-sight velocity distribution derived with Unresolved Gaussian Decomposition Method (Kuijken & Merrifield 1993). For $|r| \lesssim 8$ arcsec the NGC 4036 line profiles are asymmetric (displaying a tail opposite to the direction of rotation) and flat-topped, as they result from the h_3 and h_4 radial profiles. The h_3 and h_4 parameters measure respectively the asymmetric and symmetric deviations of the line profile from a Gaussian (Gerhard 1993; van der Marel & Franx 1993). For NGC 4036 the h_3 term anticorrelates with v, rising to $\sim+0.1$ in the approaching side and falling to ~-0.1 in the receding side. The h_4 term exhibits a negative value (~-0.03).

3 MODELLING THE STELLAR KINEMATICS

3.1 Modelling technique

We built an axisymmetric bulge–disc dynamical model for NGC 4036 by applying the Jeans modelling technique introduced by Binney, Davies & Illingworth (1990), developed by van der Marel, Binney & Davies (1990) and van der Marel (1991), and extended to two-component galaxies by CvdM94 and to galaxies with a DM halo by Cinzano (1995) and Corsini et al. (1999). For details the reader is referred the above references.

The main steps of the adopted modelling are (i) the calculation of the bulge and disc contribution to the potential from the observed surface brightness of NGC 4036, (ii) the solution of the Jeans equations to obtain separately the bulge and disc dynamics in the total potential, and (iii) the projection of the derived dynamical quantities on to the sky-plane taking into account seeing effects, instrumental set-up and reduction technique to compare the model predictions with the measured stellar kinematics. In the following each invidual step is briefly discussed.

(i) We model NGC 4036 with an infinitesimally thin exponential disc in its equatorial plane. The disc surface mass density is specified for any inclination i, central surface brightness μ_0, scalelength r_d and constant mass-to-light ratio $(M/L)_\mathrm{d}$. The disc potential is calculated from the surface mass density as in Binney & Tremaine (1987). The limited extension of our kinematical data (measured out $r < 30$ arcsec $\simeq 0.5R_\mathrm{opt}$)[5] prevents us from disentangling in the assumed constant mass-to-light ratios the possible contribution of a dark matter halo. The surface brightness of the bulge is obtained by subtracting the disc contribution from the total observed surface brightness. The three-dimensional luminosity density of the bulge is obtained by deprojecting its surface brightness by an iterative method based on the Richardson–Lucy algorithm (Richardson 1972; Lucy 1974). Its three-dimensional mass density is derived by assuming a constant mass-to-light ratio $(M/L)_\mathrm{b}$. The potential of the bulge is derived solving the Poisson equation by a multipole expansion (e.g. Binney & Tremaine 1987).

(ii) The bulge and disc dynamics are derived by separately solving the Jeans equations for each component in the total potential of the galaxy. For both components we assume a two-integral distribution function of the form $f = f(E, L_z)$. This implies that the vertical velocity dispersion σ_z^2 is equal to second radial velocity moment σ_R^2, and that $\overline{v_R v_z} = 0$. Therefore the Jeans equations becomes a closed set, which can be solved for the unknowns $\overline{v_\phi^2}$ and $\sigma_R^2 = \sigma_z^2$. Other assumptions to close the Jeans equations are also possible (e.g. van der Marel & Cinzano 1992).

For the bulge we made the same hypotheses of Binney, Davies & Illingworth (1990). A portion of the second velocity moment $\overline{v_\phi^2}$ is assigned to bulge streaming velocity $\overline{v_\phi}$, following Satoh's (1980) prescription.

For the disc we made the same hypotheses of Rix & White (1992) and CvdM94. The second radial velocity moment σ_R^2 in the disc is assumed to fall off exponentially with a scalelength R_σ from a central value of $\sigma_{\mathrm{d}0}^2$. The azimuthal velocity dispersion σ_ϕ^2 in the disc is assumed to be related to σ_R^2 according to the relation from epicyclic theory (cf. equation 3-76 of Binney & Tremaine 1987). As pointed out by CvdM94, this relation may introduce systematic errors (Kuijken & Tremaine 1992; Evans & Collett 1993; Cuddeford & Binney 1994). The disc streaming velocity $\overline{v_\phi}$ (i.e., the circular velocity corrected for the asymmetric drift) is determined by the Jeans equation for radial equilibrium.

(iii) We projected back on to the plane of the sky (at the given inclination angle) the dynamical quantities of both the bulge and the disc to find the line-of-sight projected streaming velocity and velocity dispersion. We assumed that both the bulge and the disc have a Gaussian line profile. At each radius their sum (normalized to the relative surface brightness of the two components) represents the model-predicted line profile. As in CvdM94, the

[5] The optical radius R_opt is the radius encompassing the 83 per cent of the total integrated light.

predicted line profiles were convolved with the seeing PSF of the spectroscopic observations and sampled over the slit width and pixel size to mimic the observational spectroscopic set-up. We mimicked the Fourier Quotient Method for measuring the stellar kinematics by fitting the predicted line profiles with a Gaussian in the Fourier space to derive the line-of-sight velocities and velocity dispersions for the comparison with the observed kinematics. The problems of comparing the true velocity moments with the Fourier Quotient results were discussed by van der Marel & Franx (1993) and by CvdM94.

3.2 Results for the stellar component

3.2.1 Seeing-deconvolution

The modelling technique described in Section 3.1 derives the three-dimensional mass distribution from the three-dimensional luminosity distribution inferred from the observed surface photometry by a fine-tuning of the disc parameters leading to the best fit on the kinematical data. We performed a seeing-deconvolution of the *V*-band image of NGC 4036 to take into account the seeing effects on the measured photometrical quantities (surface brightness, ellipticity and cos 4θ deviation profiles) used in the deprojection of the two-dimensional luminosity distribution. We obtained a restored NGC 4036 image through an iterative method based on the Richardson–Lucy algorithm (Richardson 1972; Lucy 1974) available in the IRAF package STSDAS. We assumed the seeing PSF to be a circular Gaussian with a FWHM = 1.7 arcsec. Noise amplification represents a main backdraw in all Richardson–Lucy iterative algorithms, and the number of iterations needed to get a good image restoration depends on the steepness of the surface-brightness profile (e.g. White 1994). After six iterations, we did not notice any more substantial change in the NGC 4036 surface-brightness profile, while the image became too noisy. We therefore decided to stop at the sixth iteration. The surface-brightness, ellipticity, position angle radial profiles of NGC 4036 after the seeing-deconvolution are displayed in Fig. 2 compared with the *HST* and the unconvolved ground-based photometry. The raises found at small radii for the surface brightness ($r \sim 0.2$ mag arcsec^{-2}) and for the ellipticity ($r \sim 0.05$) are comparable in size to the values found by Peletier et al. (1990) for seeing effects in the centre of ellipticals.

3.2.2 Bulge–disc decomposition

We performed a standard bulge–disc decomposition with a parametric fit (e.g. Kent 1985) in order to find a starting guess for the exponential disc parameters to be used in the kinematical fit. We decomposed the seeing-deconvolved surface-brightness profile on both the major and the minor axes as the sum of an $R^{1/4}$ bulge, having a surface-brightness profile

$$\mu_{\rm b}(r) = \mu_{\rm e} + 8.3268\left[\left(\frac{r}{r_{\rm e}}\right)^{1/4} - 1\right], \qquad (1)$$

plus an exponential disc, having a surface-brightness profile

$$\mu_{\rm d}(r) = \mu_0 + 1.0857\left(\frac{r}{r_{\rm d}}\right). \qquad (2)$$

We assumed that the minor-axis profile of each component is the same as the major-axis profile, but scaled by a factor $1 - \epsilon = b/a$.

Table 1. The bulge-disc decomposition parameters.

	bulge			disc		
	$\mu_{\rm e}$	$r_{\rm e}$	ϵ	μ_0	$r_{\rm d}$	i
this paper	20.4	12.″8	0.11	18.7	22.″1	74.°9
Kent (1985)	20.7	13.″1	0.07	18.6	21.″0	71.°9

Note: $\mu_{\rm e}$ and μ_0 are given in *V* mag arcsec^{-2}. Kent's (1985) surface brightnesses have been converted from the *r* band to the *V* band.

A least-squares fit of the photometric data provides $\mu_{\rm e}$, $r_{\rm e}$ and ϵ of the bulge, μ_0, $r_{\rm d}$ of the disc, and the galaxy inclination i (see Table 1 for the results).

Kent (1984) measured surface photometry of NGC 4036 in the *r* band. He decomposed the major- and minor-axis profiles in an $R^{1/4}$ bulge and in an exponential disc (Kent 1985). A rough but useful comparison between the bulge and disc parameters resulting from the two photometric decompositions is possible by a transformation from the *r* band to the *V* band of Kent's data. We derived from Kent's surface brightness profile along the major axis of NGC 4036 its (extrapolated) total magnitude $r_T = 10.56 \pm 0.02$ corresponding to $V_T - r_T = 0.13 \pm 0.11$. Then we converted the μ_0 and $\mu_{\rm e}$ values from the *r* band to the *V* band (see Table 1). The differences between the best-fitting parameters obtained from the two decompositions are lower than 10 per cent except for bulge ellipticity (our value is ~ 64 per cent than the Kent's one). These discrepancies are consistent with the differences in the slope of the two surface-brightness profiles, with the different approaches to correct for the seeing effects (Kent 1985 convolved the theoretical bulge and disc profiles with the observed Gaussian seeing profile) and with the uncertainties of the conversion from the *r* band to the *V* band of Kent's surface brightnesses.

3.2.3 Modelling results

We looked for the disc parameters leading to the best fit of the observed stellar kinematics, using as a starting guess those resulting from our best-fitting photometric decomposition, with $|\mu_0 - 1 \text{ mag arsec}^{-2}| \leq 18.7$ mag arcsec^{-2}, $|r_{\rm d} - 5 \text{ arcsec}| \leq 22.1$ arcsec, and $|i - 5°| \leq 74.°9$. For any exponential disc of fixed μ_0, $r_{\rm d}$, i (in the investigated range of values), we subtracted its surface brightness from the total seeing-deconvolved surface brightness. The residual surface brightness was considered to be contributed by the bulge. Since μ_0, $r_{\rm d}$ and i are correlated, a bulge component with a surface-brightness profile consistent with that resulting from the photometric decomposition was obtained only by taking exponential discs characterized by large μ_0 values in combination with large values of $r_{\rm d}$ (i.e., larger but fainter discs) or by small μ_0 and small $r_{\rm d}$ (i.e., smaller but brighter discs). After subtracting the disc contribution to the total surface brightness, the three-dimensional luminosity density of the bulge was obtained after seven Richardson–Lucy iterations, starting from a fit to the actual bulge surface brightness with the projection of a flattened Jaffe profile (1983). The residual surface brightness ($\Delta\mu = \mu_{\rm model} - \mu_{\rm obs}$) after each iteration and the final three-dimensional luminosity density profiles of the spheroidal component of NGC 4036 along the major, the minor and two intermediate axes are plotted for the kinematical best-fitting model in Fig. 7 up to 100 arcsec (the stellar and ionized-gas kinematics are measured to $\sim$30 arcsec).

We applied the modelling technique described in Section 3.1, considering only models in which the bulge is an oblate isotropic

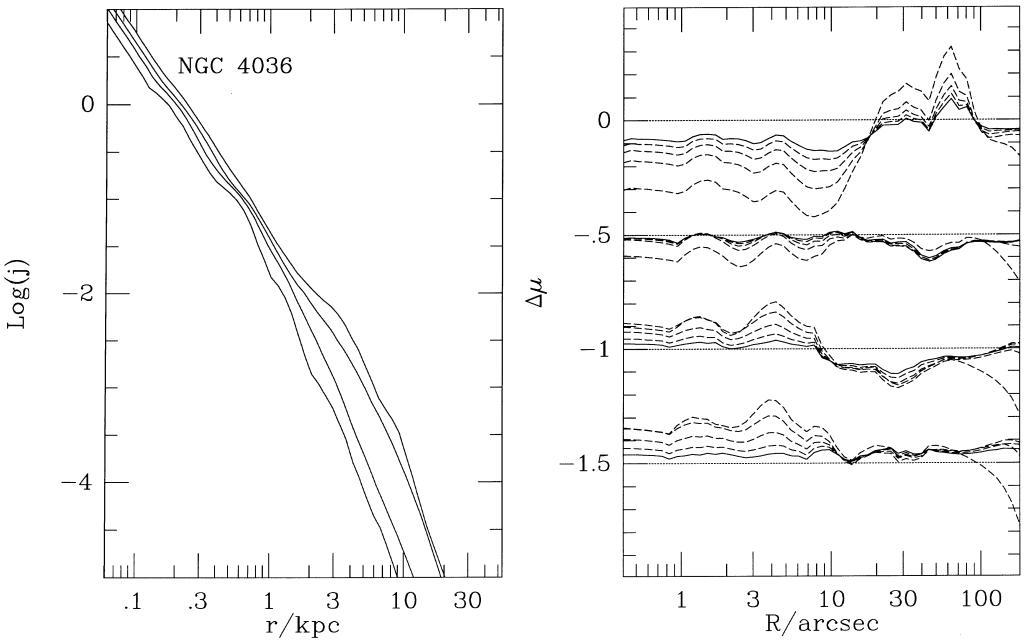

Figure 7. The deprojection of the surface brightness of the spheroidal component of the NGC 4036 for the best-fitting kinematical model. The right-hand panel shows the residual surface brightness $\Delta\mu$ in mag arcsec^{-2} after each Lucy iteration (dashed lines) from an initial Jaffe fit to the actual NGC 4036 bulge brightness. The residuals are shown for four axes (major to minor axis: top to bottom). For each set of curves the solid line corresponds to the projected adopted model for the three-dimensional luminosity density and the dotted line corresponds to a perfect deprojection. At each interaction, if the model is brighter than the galaxy, the corresponding dashed or continuous curve is below the dotted line. In the left-hand panel the final three-dimensional luminosity density profile of the spheroidal component of the NGC 4036 right-hand panel is given in units of $10^{10}\,\mathrm{L}_{\odot}\,\mathrm{kpc}^{-3}$ for the same four axes (minor to major axis: innermost to outermost curve).

rotator (i.e., $k = 1$), and in which the bulge and the disc have the same mass-to-light ratio $(M/L)_\mathrm{b} = (M/L)_\mathrm{d}$. The *M/L* determines the velocity normalization, and was chosen (for each combination of disc parameters) to optimize the fit to the rms velocity profile. The best-fitting model to the observed major-axis stellar kinematics is obtained with a mass-to-light ratio $M/L_V = 3.42\,\mathrm{M}_{\odot}/\mathrm{L}_{\odot V}$ and with an exponential disc having a surface-brightness profile

$$\mu_\mathrm{d}(r) = 19.3 + 1.0857\left(\frac{r}{22.0\,\mathrm{arcsec}}\right)\,\mathrm{mag\,arcsec}^{-2}, \qquad (3)$$

(represented by the dashed line in the top panel of Fig. 1), a radial velocity dispersion profile

$$\sigma_R(r) = 155\,\mathrm{e}^{-r/27''.4}\,\mathrm{km\,s}^{-1}, \qquad (4)$$

(where the galactocentric distance r is expressed in arcsec) and an inclination $i = 72°$. Fig. 8 shows the comparison between the rotation curve, the dispersion velocity profile and the rms velocity curve predicted by the best-fitting model (solid lines) with the observed stellar kinematics along the major axis of NGC 4036. The agreement is good.

The derived *V*-band luminosities for bulge and disc are $L_\mathrm{b} = 2.8\times10^{10}\,\mathrm{L}_{\odot V}$ and $L_\mathrm{d} = 1.4\times10^{10}\,\mathrm{L}_{\odot V}$. They correspond to the masses $M_\mathrm{b} = 9.8\times10^{10}\,\mathrm{M}_{\odot}$ and $M_\mathrm{d} = 4.8\times10^{10}\,\mathrm{M}_{\odot}$. The total ?tlsb=-.1pt>mass of the galaxy (bulge + disc) is $M_T = 14.5\times10^{10}\,\mathrm{M}_{\odot}$. The disc-to-bulge and disc-to-total *V*-band luminosity ratios are $L_\mathrm{b}/L_\mathrm{d} = 0.58$ and $L_\mathrm{d}/L_T = 0.36$. The disc-to-total luminosity ratio as function of the galactocentric distance is plotted in Fig. 9.

3.2.4 *Uncertainty ranges for the disc parameters*

The uncertainty ranges for the disc parameters are $19.1 \lesssim \mu_0 \lesssim 19.5\,\mathrm{mag\,arcsec}^{-2}$, $20 \lesssim r_\mathrm{d} \lesssim 24\,\mathrm{arcsec}$ and $71° \lesssim i \lesssim 73°$. In Fig. 10 the continuous and the dotted lines show the kinematical profiles predicted for two discs with the same inclination ($i = 72°$) and the same total luminosity of the best-fitting disc but with a smaller ($\mu_0 = 19.1\,\mathrm{mag\,arcsec}^{-2}$, $r_\mathrm{d} = 20.0\,\mathrm{arcsec}$) or greater ($\mu_0 = 19.5\,\mathrm{mag\,arcsec}^{-2}, r_\mathrm{d} = 24.0\,\mathrm{arcsec}$) scalelength respectively. In Fig. 11 the continuous and the dotted lines correspond to two discs with the same scalelength ($r_\mathrm{d} = 22.0\,\mathrm{arcsec}$) of the best-fitting disc but with a lower ($\mu_0 = 19.2\,\mathrm{mag\,arcsec}^{-2}$, $i = 71°$) or a higher ($\mu_0 = 19.4\,\mathrm{mag\,arcsec}^{-2}$, $i = 73°$) inclination. Their total luminosity is respectively ~14 per cent lower and ~16 per cent higher than that of the best-fitting disc. The fits of these models to the data are also acceptable, so we estimate a ~15 per cent error in the determination of the disc luminosity and mass. The good agreement with observations obtained with $k = 1, (M/L)_\mathrm{b} = (M/L)_\mathrm{d}$, and without a dark matter halo causes us not to investigate models with $k \neq 1, (M/L)_\mathrm{b} \neq (M/L)_\mathrm{d}$ or with radially increasing mass-to-light ratios. Therefore we cannot exclude them at all.

The *V*-band luminosity (after inclination correction) of the exponential disc corresponding to the model best fitted to the observed stellar kinematics is ~75 per cent than that of the disc obtained from the parametric fit of the surface-brightness profiles. The differences between the disc parameters derived from NGC 4036 photometry ($\mu_0 = 18.7\,\mathrm{mag\,arcsec}^{-2}$, $r_\mathrm{d} = 22.1\,\mathrm{arcsec}, i = 74°.9$) and from the stellar kinematics ($\mu_0 = 19.3\,\mathrm{mag\,arcsec}^{-2}$, $r_\mathrm{d} = 22.0\,\mathrm{arcsec}, i = 72°$) are as expected. In fitting the NGC

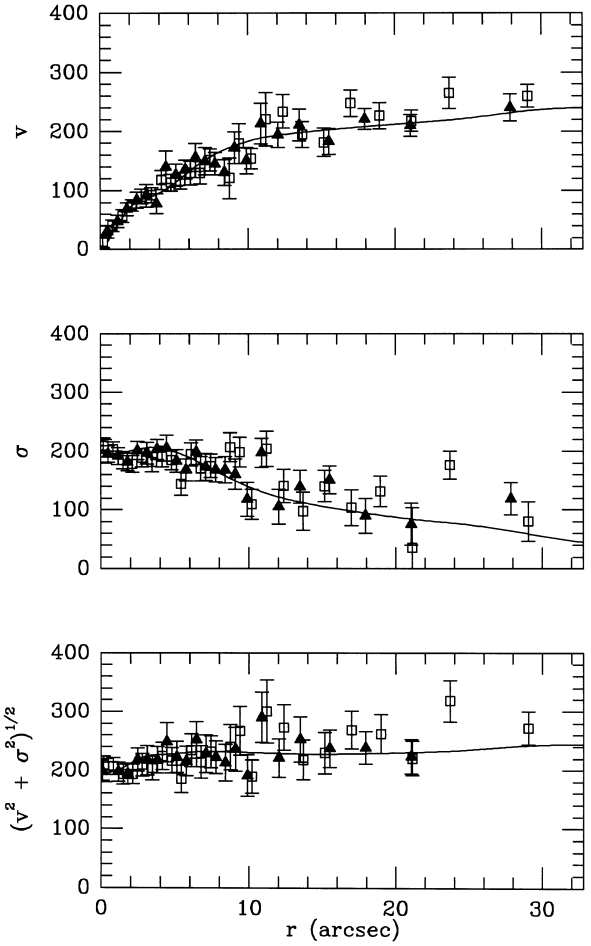

Figure 8. Comparison of the model predictions to the stellar major-axis kinematics for NGC 4036. Data points are as in Fig. 4. The solid curves represent the velocity (top panel), velocity dispersion (middle panel) and rms velocity (bottom panel) radial profiles of the best-fitting model (in which the disc parameters are $\mu_0 = 19.3\,\mathrm{mag\,arcsec^{-2}}$, $r_\mathrm{d} = 22.0\,\mathrm{arcsec}$ and $i = 72°$).

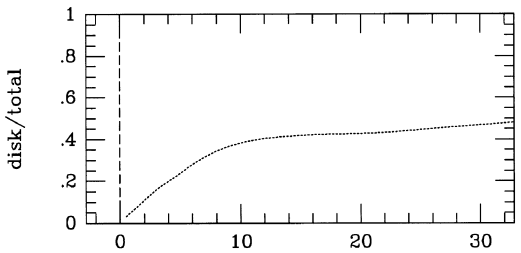

Figure 9. Radial profile of the fraction of the light contributed by the stellar disc along the major axis of NGC 4036 as obtained by the best-fitting model. The distance from the centre is expressed in arcsec.

4036 surface-brightness profiles the bulge is assumed (i) to be axisymmetric, (ii) to have a $R^{1/4}$ profile; and (iii) and to have constant axial ratio (i.e., its isodensity luminosity spheroids are similar concentric ellipsoids). We adopted this kind of representation for the bulge component only to find rough bounds on the exponential disc parameters to be used in the kinematical fit. Often bulges have neither an $R^{1/4}$ law profile

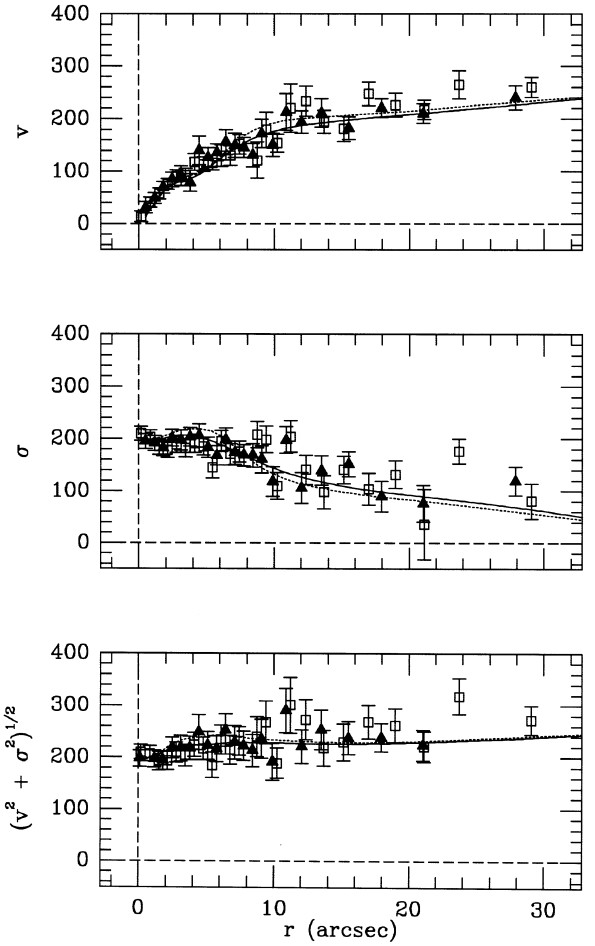

Figure 10. As in Fig. 8, but for a disc with $\mu_0 = 19.1\,\mathrm{mag\,arcsec^{-2}}$, $r_\mathrm{d} = 20.0\,\mathrm{arcsec}$ and $i = 72°$ (continuous line) and for a disc with $\mu_0 = 19.5\,\mathrm{mag\,arcsec^{-2}}$, $r_\mathrm{d} = 24.0\,\mathrm{arcsec}$ and $i = 72°$ (dotted line).

(e.g. Burstein 1979; Simien & Michard 1984) nor perfectly elliptical isophotes (e.g. Scorza & Bender 1990). Therefore in modelling the stellar kinematics the three-dimensional luminosity density j_b of the stellar bulge is assumed (i) to be oblate axisymmetric, but (ii) not to be parametrized by any analytical expression, (iii) nor to have isodensity luminosity spheroids with constant axial ratio. The flattening of the spheroids increases with the galactocentric distance, as it appears from the three-dimensional luminosity density profiles plotted in Fig. 7 along different axes on to the meridional plane of NGC 4036. This flattening produces an increasing of the streaming motions for the bulge component assumed to be an isotropic rotator.

3.2.5 Modelling results with stellar kinematics by Fisher (1997)

The bulge and disc parameters found for our best-fitting model reproduce also the major-axis stellar kinematics by F97. Rather than choosing an 'ad hoc' wavenumber range to emulate F97 analysis technique, the fit to the predicted line profile was done in ordinary space and not in the Fourier space as was done to reproduce our Fourier Quotient measurements. The good agreement of the resulting kinematical profiles with F97 measurements is shown in Fig. 12.

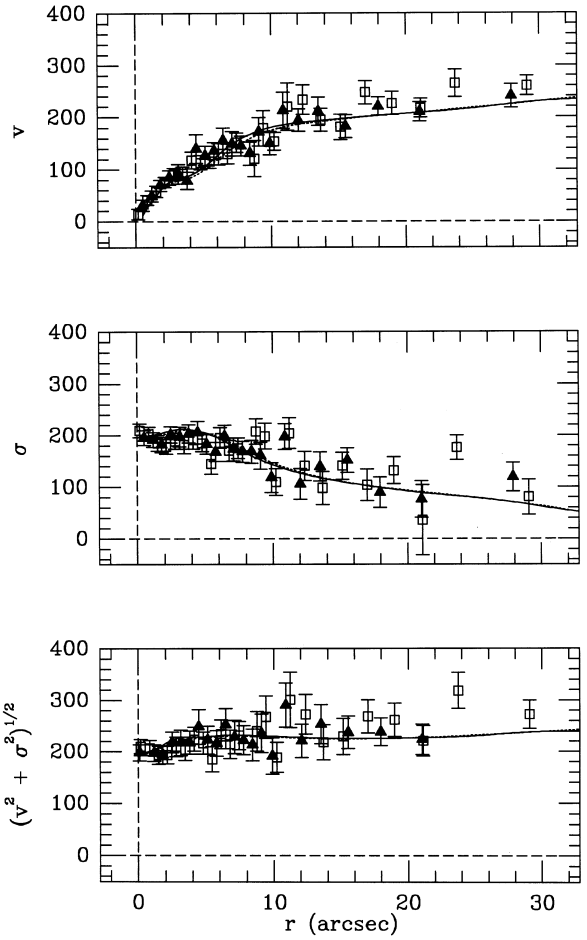

Figure 11. As in Fig. 8, but for a disc with $\mu_0 = 19.2\,\mathrm{mag\,arcsec^{-2}}$, $r_\mathrm{d} = 22.0\,\mathrm{arcsec}$ and $i = 71°$ (continuous line) and for a disc with $\mu_0 = 19.4\,\mathrm{mag\,arcsec^{-2}}$, $r_\mathrm{d} = 22.0$ and $i = 73°$ (dotted line).

4 MODELLING OF THE IONIZED GAS KINEMATICS

4.1 Modelling technique

At small radii both the ionized gas velocity and velocity dispersion are comparable to the stellar values, for $r \leq 9$ arcsec and $r \leq 5$ arcsec respectively. This prevented us from modelling the ionized gas kinematics by assuming that the gas had settled into a disc component, as was done by CvdM94 for NGC 2974. Moreover, a change in the slope of the [O II] λ3726.2 intensity radial profile (Fig. 6) is observed at $r \lesssim 8$ arcsec, and its gradient appears to be somewhat steeper towards the centre. The velocity dispersion and intensity profiles of the ionized gas suggest that it is distributed into two components (see also the distinct central structure in the *HST* Hα+[N II] image, Fig. 3): a small inner spheroidal component and a disc.

We built a dynamical model for the ionized gas with a dynamically hot spheroidal and in a dynamically colder disc component.

The total mass of the ionized gas $M_\mathrm{H\,II}$ is negligible, and the total potential is set only by the stellar component. The mass of the ionized gas can be derived from optical recombination line theory (see Osterbrock 1989) by the Hα luminosity. For a given

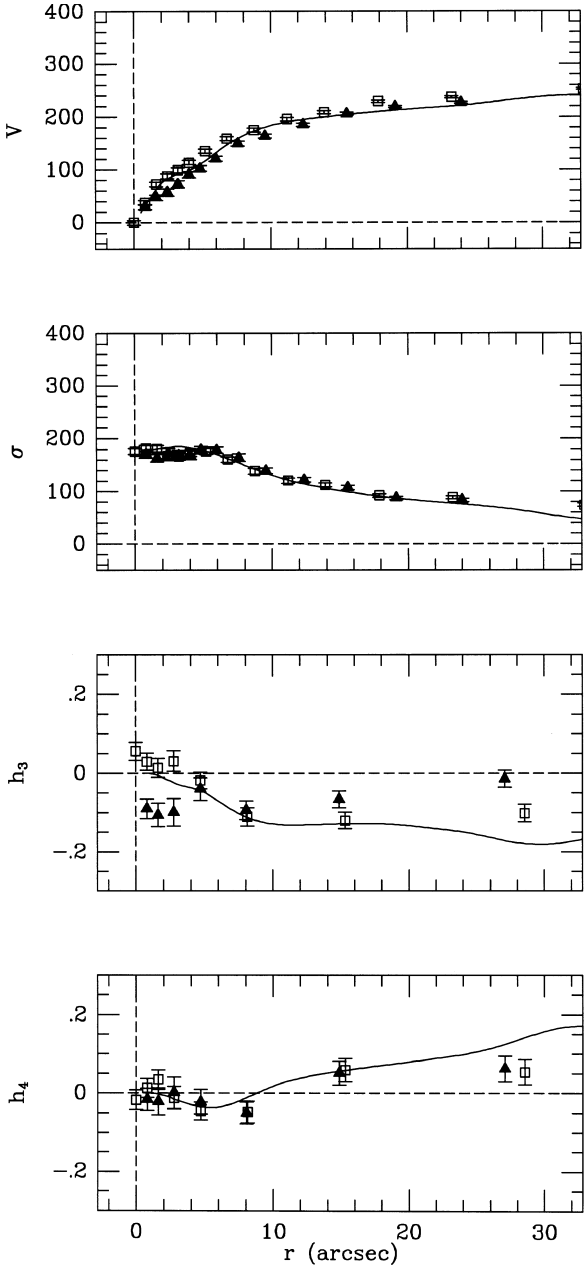

Figure 12. Comparison of the predictions of the same model as in Fig. 8 with the stellar major-axis kinematics for NGC 4036 by Fisher (1997). Data points are as in Fig. 4. The solid curves represent the velocity v, velocity dispersion σ, h_3 and h_4 radial profiles of the best-fitting model, taking into account the Fisher's data reduction technique.

electron temperature T_e and density N_e, the H II mass is given by

$$M_\mathrm{H\,II} = \left(L_{\mathrm{H}\alpha} m_\mathrm{H}/N_\mathrm{e}\right)/\left(4\pi j_{\mathrm{H}\alpha}/N_\mathrm{e}N_\mathrm{p}\right), \quad (5)$$

where $L_{\mathrm{H}\alpha}$ is the Hα luminosity, m_H is the mass of the hydrogen atom, $j_{\mathrm{H}\alpha}$ is the Hα emissivity, and N_p is the proton density (Tohline & Osterbrock 1976). The Hα luminosity of NGC 4036 scaled to the adopted distance is $L_{\mathrm{H}\alpha} = 5.6 \times 10^{39}\,\mathrm{L_\odot}$ (Ho, Filippenko & Sargent 1997). The term $4\pi j_{\mathrm{H}\alpha}/N_\mathrm{e}N_\mathrm{p}$ is insensitive to changes of N_e over the range 10^2–$10^6\,\mathrm{cm^{-3}}$. It decreases by a factor of 3 for changes of T_e over the range 5×10^3 –$2\times10^4\,\mathrm{K}$ (Osterbrock 1989). For an assumed temperature $T_\mathrm{e} = 10^4\,\mathrm{K}$, the

electron density is estimated to be $N_e = 2 \times 10^2\,cm^{-3}$ from the [S II] ratio found by Ho et al., implying $M_{H\,II} = 7 \times 10^4\,M_\odot$.

For the gaseous spheroid and disc we made two different sets of assumptions based on two different physical scenarios for the gas cloudlets.

4.1.1 *Long-lived gas cloudlets (model A)*

In a first set of models we described the gaseous component by a set of collisionless cloudlets in hydrostatic equilibrium. The small gaseous 'spheroid' is characterized by a density distribution and flattening different from those of stars. Its major-axis luminosity profile was assumed to follow an $R^{1/4}$ law. Adopting for it Ryden's (1992) analytical approximation, we obtained the three-dimensional luminosity density of the gaseous spheroid. The flattening of the spheroids q was kept as free parameter. To derive the kinematics of the gaseous spheroid, we solved the Jeans equations under the same assumptions as were made in Section 3 for the stellar spheroid. In particular, the streaming velocity $\overline{v_\phi}$ of gaseous bulge is derived from the second azimuthal velocity moment $\overline{v_\phi^2}$ using Satoh's (1980) relation. For the ionized gaseous disc we solved the Jeans equations under similar assumptions as those made in Section 3 for the stellar disc. Specifically, we assumed that the gaseous disc (i) has an exponential luminosity profile, (ii) is infinitesimally thin, (iii) has an exponentially decreasing σ_R^2, (iv) has $\sigma_z^2 = \sigma_R^2$, and (v) has σ_ϕ^2 satisfying the epicyclic relation.

4.1.2 *Gas cloudlets 'just' shed by the stars (model B)*

In a second set of models we assumed that the emission observed in the gaseous spheroid and disc arises from material that was recently shed from stars. Different authors (Bertola et al. 1984; Fillmore, Boroson & Dressler 1986; Kormendy & Westpfahl 1989; Mathews 1990) suggested that the gas lost (e.g. in planetary nebulae) by stars was heated by shocks to the virial temperature of the galaxy within 10^4 yr, a time shorter than the typical dynamical time of the galaxy. Hence in this picture the ionized gas and the stars have the same true kinematics, while their observed kinematics are different due to the line-of-sight integration of their different spatial distribution. Differences between the radial profiles of the gas emissivity and the stellar luminosity may be explained if both the gas emission process and the efficiency of the thermalization process show a variation with the galactocentric distance. The three-dimensional luminosity density of the spheroid is derived as in model A, and the luminosity density profile of the disc is assumed to be exponential.

In both cases, the kinematics of the gaseous spheroid and disc were projected on to the sky-plane to be compared to the observed ionized gas kinematics. Assuming a Gaussian line profile for both the gaseous components, we derived the total line profile (which depends on the relative flux of the two components). As for the stellar components, we convolved the line profiles obtained for the ionized gas with the seeing PSF, and we sampled them over the slit-width and pixel size to mimic the observational set-up. This procedure is particularly important for the modelling of the observed kinematics near the centre. As a last step (in mimicking the measuring technique of the gaseous kinematics) we fitted a single Gaussian to the resulting line profile, after taking into account the instrumental line profile.

4.2 Results for the gaseous component

We decomposed the [O II] λ3726.2 intensity profile as the sum of an $R^{1/4}$ gaseous spheroid and an exponential gaseous disc. A least-squares fit of the observed data was done for $r > 3$ arcsec to deal with seeing effects (Fig. 6). The gas spheroid turned out to be the dominating component up to $r \sim 8$ arcsec beyond the bright emission in Fig. 3. We derived the effective radius of the gaseous spheroid $r_{e,gas} = 0.5 \pm 0.1$ arcsec, the scalelength of the gaseous disc $r_{d,gas} = 29.8 \pm 0.9$ arcsec, and the ratio of the effective intensity of the spheroid to the central intensity of the disc $I_{e,gas}/I_{0,gas} = 718^{+813}_{-153}$. The uncertainties on the resulting parameters have been estimated by a separate decomposition on each side of the galaxy. With these parameters we applied the models for the gas kinematics described in Section 4.1.

Since in both models A and B the stellar density radial profile differs from the gas emissivity radial profile, it is interesting to check what is the relation between the three-dimensional stellar density $\rho_{star}(R)$ and the three-dimensional gas emissivity $\nu_{gas}(R)$. After deprojection, we find that they are related by the relation

$$\nu_{gas}(R) \propto \rho_{star}^{2.3}(R) \tag{6}$$

in the range of galactocentric distances between $r \sim 2$ and $\sim$10 arcsec. In a fully ionized gas the recombination rate is proportional to the square of the gas density (e.g. Osterbrock 1989); this is a power-law relation quite similar to equation (6).

For models A and B the best fits to the observed gas kinematics are in both cases obtained with a spheroid flattening $q = 0.8$, and are plotted respectively in Figs 13 and 14. The best result is obtained with model B. A simple estimate of the errors on the model due to the uncertainties of bulge–disc decomposition of the radial profile of [O II] λ3726.2 emission line can be inferred by comparing the model predictions based on the separate decomposition on each side of the galaxy. We find a maximum difference of 5 per cent for $4 < r < 10$ arcsec between the gas velocities and velocity dispersion predicted using the two different bulge–disc decompositions of the [O II] λ3726.2 intensity profile. For model A the assumption of Satoh's (1980) relation fails in reproducing the observed gas kinematics for $r \lesssim 6$ arcsec, where the emission-line intensity profile is dominated by the gaseous spheroidal component. However, the $R^{1/4}$ extrapolation of the density profile in the inner 3 arcsec overestimates the density gradient in this region (as it appears also from the *HST* image; Fig. 3) which could produce an exceedingly asymmetric drift correction.

4.2.1 *Modelling results with gas kinematics by Fisher (1997)*

We also applied our models A and B to the ionized gas kinematics and to the [O III] λ5006.9 intensity radial profile measured by F97 along the major axis of NGC 4036. The best fits to F97 data for models A and B are obtained with a spheroid flattening $q = 0.8$. They are shown in Figs 15 and 16 respectively.

In this case the dynamical predictions of model B (even if they give better results than those of model A) are not able to reproduce the F97's kinematics in the radial range between 3 and 10 arcsec. The differences between the predicted and the measured kinematics rise up to 80 km s^{-1} in velocities and to 40 km s^{-1} in velocity dispersions at $r \sim 6$ arcsec. Nevertheless, for $0 < r < 10$ arcsec this model agrees better with the observations than if the gas is assumed to be on circular orbits (see the dotted lines in

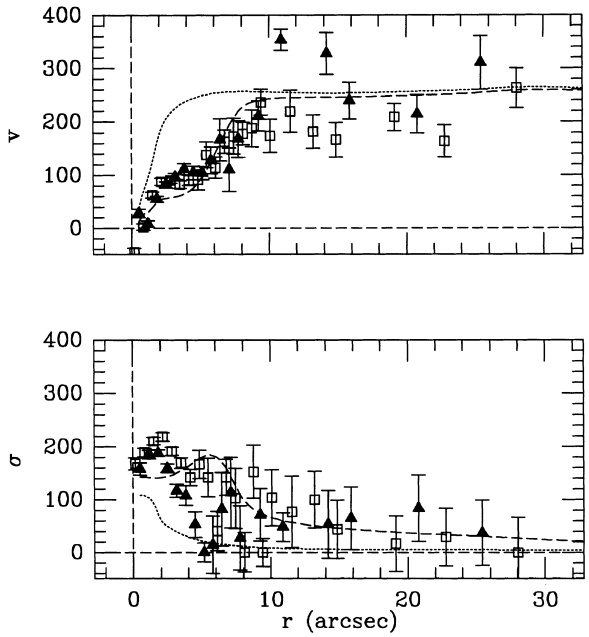

Figure 13. Comparison of the predictions of model A (dashed curve) to the ionized gas kinematics observed along the major axis of NGC 4036. The data points are as in Fig. 5. The dotted curves represent the seeing-convolved circular velocity curve and zero velocity-dispersion profile in the galaxy meridional plane.

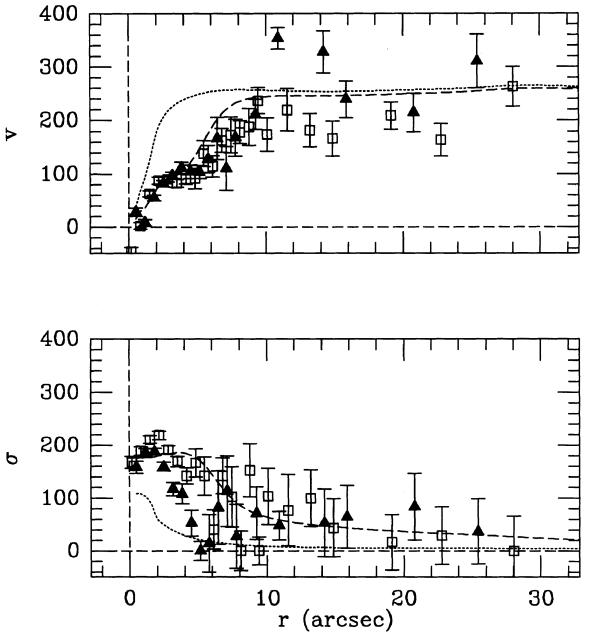

Figure 14. As in Fig. 13, but for model B.

Fig. 16). If this is the case, the maximum differences with the measured kinematics are as large as $130\,\mathrm{km\,s^{-1}}$ in velocity and as $110\,\mathrm{km\,s^{-1}}$ in velocity dispersion for $r \sim 4$ arcsec.

4.3 Do drag forces affect the kinematics of the gaseous cloudlets?

Considerable differences exist between the ionized gas kinematics recently measured by F97 and the velocity and velocity dispersion

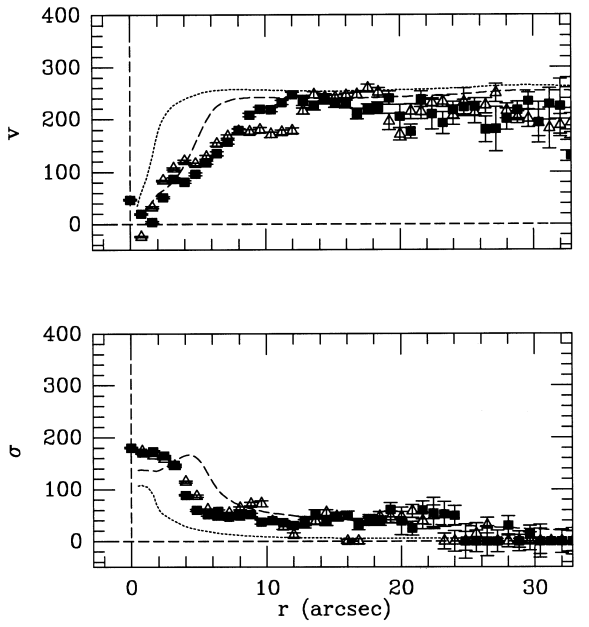

Figure 15. As in Fig. 13, but for the gas kinematics measured by Fisher (1997). Open triangles and filled squares represent data derived for the approaching west and receding east sides respectively.

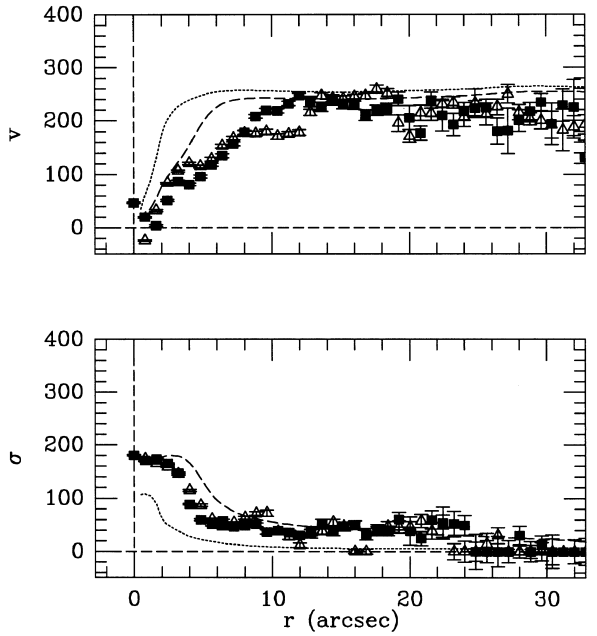

Figure 16. As in Fig. 15, but for model B.

profiles predicted even by the best model in the bulge-dominated region between $r \sim 4$ and $r \sim 10$ arcsec. This suggests that other phenomena play a role in determining the dynamics of the spheroid gas [see item (iii) in Section 1]. The discrepancy between the model and observations could be explained by accounting for the drag interaction between the ionized gas and the hot component of the interstellar medium.

In the scenario of evolution for stellar ejecta in elliptical galaxies outlined by Mathews (1990), a portion of the gas shed by stars (e.g., as stellar winds or planetary nebulae) undergoes to an orbital separation from its parent stars by the interaction with

ambient gas, after an expansion phase and the attainment of pressure equilibrium with the environment, and before its disruption by various instabilities. Indeed, to explain the luminosity of the optical emission lines measured for nearby ellipticals, Mathews estimated that the ionized gas ejected from the orbiting stars merges with the hot interstellar medium in at least $t_{\rm life}\sim10^6$ yr. If the gas clouds have at the beginning the same kinematics of their parent stars, this lifetime is sufficiently long to let the gaseous clouds (which start with the same kinematics of their parent stars) to acquire an own kinematical behaviour due to the deceleration produced by the drag force of the diffuse interstellar medium. The lifetime of the ionized gas nebulae is shorter than 10^4–10^5 yr if magnetic effects on gas kinematics are ignored (as in our model B).

To obtain some qualitative insights in understanding the effects of a drag force on the gas kinematics, we studied the case of a gaseous nebula moving in the spherical potential

$$\Phi(r)=\frac{4}{3}\pi G\rho r^2, \tag{7}$$

generated by an homogeneous mass distribution of density ρ and which, starting on to a circular orbit, is decelerated by a drag force

$$\boldsymbol{F}_{\rm drag}=-\frac{k_{\rm drag}}{m}v^2\frac{\boldsymbol{v}}{v}, \tag{8}$$

where m and $\boldsymbol{v}$ are the mass and the velocity of the gaseous cloud. Following Mathews (1990), the constant $k_{\rm drag}$ is given by

$$k_{\rm drag}\approx\frac{3}{4}\frac{n}{n_{\rm eq}}\frac{m}{a_{\rm eq}}, \tag{9}$$

where n is the density of the interstellar medium, and $n_{\rm eq}$ and $a_{\rm eq}$ are respectively the density and the radius of the gaseous nebula when the equilibrium is reached between the internal pressure of the cloud and the external pressure of the interstellar medium. The ratio $n/n_{\rm eq}\sim10^{-3}$ at any galactic radius, and therefore the ratio $k_{\rm drag}/m$ depends on the nebula radius $a_{\rm eq}$ (Mathews 1990).

The equations of motion of the nebula expressed in plane polar coordinates (r,ψ) in which the centre of attraction is at $r=0$ and ψ is the azimuthal angle in the orbital plane are

$$\ddot{r}-r\dot{\psi}^2=-\frac{4}{3}\pi G\rho r+\frac{k_{\rm drag}}{m}\dot{r}^2(r>0), \tag{10}$$

$$r\ddot{\psi}+2\dot{\psi}\dot{r}=-\frac{k_{\rm drag}}{m}r^2\dot{\psi}^2(r>0). \tag{11}$$

We numerically solved equations (10) and (11) by the Runge–Kutta method (Press et al. 1986) to study the time-dependence of the radial and tangential velocity components $\dot{r}$ and $r\dot{\psi}$ of the nebula. We fixed the potential assuming a circular velocity of $250\,{\rm km\,s^{-1}}$ at $r=1$ kpc. Following Mathews (1990), we took an

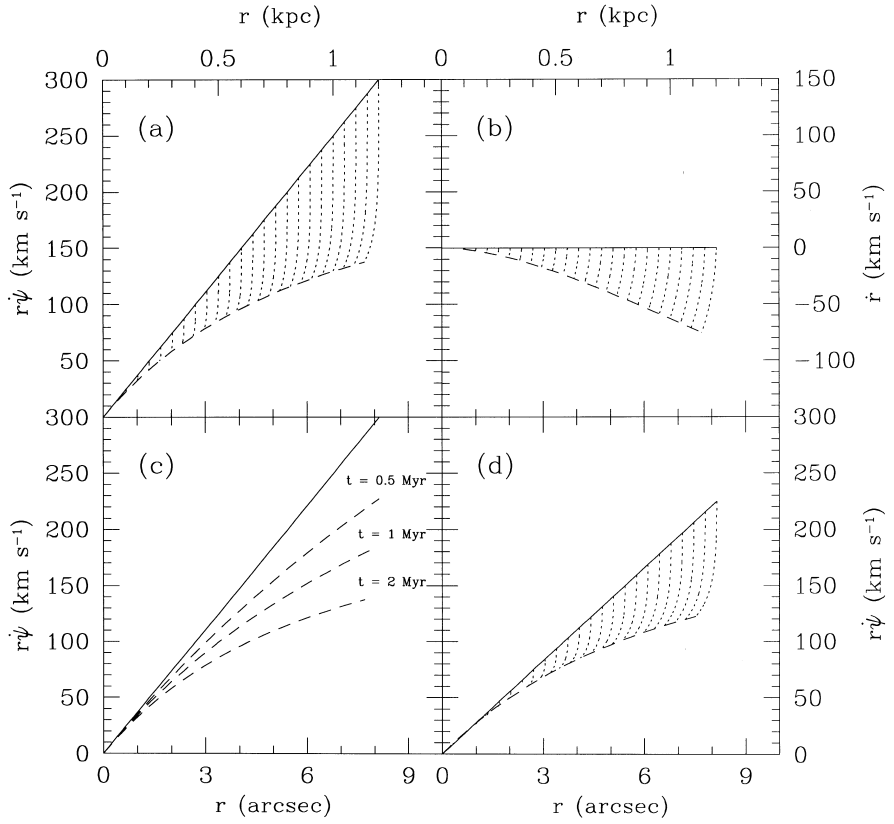

Figure 17. (a) and (b) Variation of the tangential and radial components of the velocity of ionized gas nebulae which are initially supposed to move at circular velocity (continuous line) in the potential of equation (7) under the effect of the drag force given by equation (8). The dashed lines represent the profiles of the tangential and radial components of the nebulae velocity as a function of the galactocentric distance after a time $t=2$ Myr. (c) The radial profile of the velocity tangential component after $t=0.5$, 1 and 2 Myr. (d) The radial profile of the velocity tangential component after $t=2$ Myr for nebulae initially moving at a velocity 0.75 times the circular one.

equilibrium radius for the gaseous nebula, $a_{eq} = 0.37$ pc. The results obtained for different times in which the drag force decelerate the gaseous clouds are shown in Fig. 17.

It turns out that $\ddot{\psi} < 0$ and $\ddot{r} > 0$: the clouds spiral towards the galaxy centre as expected. Moreover, the drag effects are greater on the more rapidly starting clouds, and are therefore negligible for the slowly moving clouds in the very inner region of NGC 4036.

If the nebulae are homogeneously distributed in the gaseous spheroid, only the tangential component $r\dot{\psi}$ of their velocity contributes to the observed velocity. No contribution derives from the radial component $\dot{r}$ of their velocities. In fact, for each nebula moving towards the galaxy centre which is also approaching to us, we expect to find along the line of sight a receding nebula which is falling to the centre from the same galactocentric distance with an opposite line-of-sight component of its $\dot{r}$.

The radial components of the cloudlet velocities (typically 30–40 km s^{-1}; see Fig. 17) are crucial for explaining the velocity dispersion profile and understanding how the difference between the observed velocity dispersions and the model B predictions arises. If the clouds are decelerated by the drag force, their orbits become more radially extended and the velocity ellipsoids acquire a radial anisotropy. This is a general effect, and it is true not only in our case in which the clouds initially moved on circular orbits. So we expect (in the region of the gaseous spheroid) the observed velocity dispersion profile to decrease more steeply than the one predicted by the isotropic model B. In fact, inside $5 \lesssim r \lesssim 10$ arcsec the F97 ionized gas data show that the gas velocity dispersion does not already exceed 50 km s^{-1}, even if its rotation curve falls below the circular velocities inferred from the stellar kinematics. Given that we do not know the lifetime and the density of the cloudlets, we cannot make a definite prediction.

The drag effects could explain the differences between the observed and predicted velocities if the decreasing of the tangential velocities (shown in Fig. 17) are considered as an upper limit.

A proper luminosity-weighted integration of the tangential velocities of nebulae along the line of sight has to be taken into account for the gaseous spheroid. Since the clouds are not all settled on a particular plane, the plotted values will be reduced by two distinct cosine-like terms, depending on the two angles fixing the position of any particular cloud.

Moreover (in the general case), the clouds are not all starting at the local circular velocity, and also at any given radius we find either 'younger' clouds (just shed from stars) and 'older' clouds, which are coming from farther regions of the gaseous spheroid and are going to be thermalized. Due to the nature of the drag force (acting much more efficiently on fast-moving particles), it is easy to understand that the fast 'younger' clouds will soon leave their harbours, while the slow 'older' clouds will spend much more time crossing these regions. For instance, in the case of nebulae shed at the local circular velocity on a given plane (described by equations (10) and (11) and shown in Fig. 17) we found that at $r = 0.96$ kpc (where the circular velocity is $\sim$230 km s^{-1}) almost half of the gas cloudlets are coming from regions between 0.97 and 1.1 kpc with tangential velocities between 150 and 127 km s^{-1}.

This scenario is applicable only outside 3 arcsec; whether it is applicable also inside the region of the central discrete structure revealed by the *HST* image in Fig. 3 is not clear.

5 DISCUSSION AND CONCLUSIONS

The modelling of the stellar and gas kinematics in NGC 4036 shows that the observed velocities of the ionized gas, moving in the gravitational potential determined from the stellar kinematics, cannot be explained without taking the gas velocity dispersion into account. In the inner regions of NGC 4036 the gas is clearly not moving at circular velocity. This finding is in agreement with earlier results on other disc galaxies (Fillmore, Boroson & Dressler 1986; Kent 1988; Kormendy & Westpfahl 1989) and ellipticals (CvdM94).

A much better match to the observed gas kinematics is found by assuming that the ionized gas is made of collisionless clouds in a spheroidal and a disc component for which the Jeans equations can be solved in the gravitational potential of the stars (i.e., model A in Section 4.1).

Better agreement with the observed gas kinematics is achieved by assuming that the ionized gas emission comes from material which has recently been shed from the bulge stars (i.e., model B in Section 4.1). If this gas is heated to the virial temperature of the galaxy (ceasing to produce emission lines) within a time much shorter than the orbital time, it shares the same true kinematics of its parent stars. If this is the case, we would observe a different kinematics for ionized gas and stars due only to their different spatial distribution. The number of emission-line photons produced per unit mass of lost gas may depend on the environment and therefore vary with the galactocentric distance. Therefore the intensity radial profile of the emission lines of the ionized gas can be different from that of the stellar luminosity. The continuum-subtracted Hα+[N II] image of the nucleus of NGC 4036 (Fig. 3) confirms that, except for the complex emission structure inside $\sim$3 arcsec, the smoothness of the distribution of the emission is as we expected for the gaseous spheroidal component.

In conclusion, the 'slowly rising' gas rotation curve in the inner region of NGC 4036 can be understood kinematically, at least in part. The difference between the circular velocity curve (inferred from the stellar kinematics) and the rotation curve measured for the ionized gas is substantially due to the high velocity dispersion of the gas.

This kinematical modelling leaves open the questions about the physical state (e.g., the lifetime of the emitting clouds) and the origin of the dynamically hot gas. We tested the hypothesis that the ionized gas is located in short-living clouds shed by evolved stars (e.g. Mathews 1990), finding a reasonable agreement with our observational data. These clouds may be ionized by the parent stars, by shocks, or by the UV-flux from hot stars (Bertola et al. 1995a). The comparison with the more recent and detailed data on gas by F97 opens wide the possibility for further modelling improvement if the drag effects on gaseous cloudlets (due to the diffuse interstellar medium) will be taken into account. These arguments indicate that the dynamically hot gas in NGC 4036 has an internal origin. This does not exclude the possibility for the gaseous disc to be of external origin, as discussed for S0 galaxies by Bertola, Buson & Zeilinger (1992).

Spectra at higher spectral and spatial resolution are needed to understand the structure of the gas inside 3 arcsec. Two-dimensional spectra could further elucidate the nature of the gas.

ACKNOWLEDGMENTS

We are indebted to Roeland van der Marel for providing for his

$f(E, L_z)$ modelling software, which became the basis of the programs package used here.

WWZ acknowledges the support of the Jubiläumsfonds der Oesterreichischen Nationalbank (grant 6323).

This research made use of NASA/IPAC Extragalactic Database (NED), which is operated by the Jet Propulsion Laboratory, California Institute of Technology, under contract with the National Aeronautics and Space Administration and of the Lyon-Meudon Extragalactic Database (LEDA) supplied by the LEDA team at the CRAL-Observatoire de Lyon (France).

REFERENCES

Bernacca P. L., Perinotto M., 1970, Contr. Oss. Astron. Asiago, 239, 1
Bertola F., Bettoni D., Rusconi L., Sedmak G., 1984, AJ, 89, 356
Bertola F., Rubin V. C., Zeilinger W. W., 1989, ApJ, 345, L29
Bertola F., Buson L. M., Zeilinger W. W., 1992, ApJ, 401, L79
Bertola F., Bressan A., Burstein D., Buson L. M., Chiosi C., di Serego Alighieri S., 1995a, ApJ, 438, 680
Bertola F., Cinzano P., Corsini E. M., Rix H. W., Zeilinger W. W., 1995b, ApJ, 448, L13
Bettoni D., Buson L. M., 1987, A&AS, 67, 341
Binney J. J., Mamon G. A., 1982, MNRAS, 200, 361
Binney J. J., Tremaine S., 1987, Galactic Dynamics. Princeton Univ. Press, Princeton
Binney J. J., Davies R. L., Illingworth G. D., 1990, ApJ, 361, 78
Burstein D., 1979, ApJ, 234, 829
Cinzano P., 1995, PhD thesis, Università di Padova
Cinzano P., van der Marel R.P., 1994, MNRAS, 270, 325 (CvdM94)
Corsini E. M., Pizzella A., Sarzi M., Cinzano P., Vega Beltrán J. C., Funes J. G., Bertola F., Persic M., Salucci P., 1999, A&A, 342, 671
Cuddeford P., Binney J. J., 1994, MNRAS, 266, 273
de Vaucouleurs G., de Vaucouleurs A., Corwin H. G. Jr., Buta R. J., Paturel H. G., Fouqué P., 1991, Third Reference Catalogue of Bright Galaxies. Springer-Verlag, New York (RC3)
Evans D. S., 1967, in Batten A. H., Heard J. F., eds, Proc. IAU Symp. 30, Determination of Radial Velocities and their Applications. Academic Press, London, p. 57
Evans N. W., Collett J. L., 1993, MNRAS, 264, 353
Fasano G., 1990, Internal Report, Astronomical Observatory, Padova
Fillmore J. A., Boroson T. A., Dressler A., 1986, ApJ, 302, 208
Fisher D., 1997, AJ, 113, 950 (F97)
Garcia A. M., 1993, A&AS, 100, 47
Gerhard O. E., 1993, MNRAS, 265, 213
Ho L. C., Filippenko A. V., Sargent W. L. W., 1997, ApJS, 112, 315
Jaffe W., 1983, MNRAS, 202, 995
Kent S. M., 1984, ApJS, 56, 105
Kent S. M., 1985, ApJS, 59, 115
Kent S. M., 1988, AJ, 96, 514
Kormendy J., Westpfahl D. J., 1989, ApJ, 338, 752
Kuijken K., Merrifield M. R., 1993, MNRAS, 264, 712
Kuijken K., Tremaine S., 1992, in Sundelius B., ed., Dynamics of Disk Galaxies. Univ. Goteborg Press, Goteborg, p. 71
Lucy L. B., 1974, AJ, 79, 745
Mathews W. G., 1990, ApJ, 354, 468
Michard R., 1993, in Danziger I. J., Zeilinger W. W., Kjär K., eds, Structure, Dynamics and Chemical Evolution of Elliptical Galaxies. ESO, Garching, p. 553
Osterbrock D. E., 1989, Astrophysics of Gaseous Nebulae and Active Galactic Nuclei. Univ. Science Books, Mill Valley
Peletier R. F., Davies R. L., Illingworth G. D., Davies L. E., Cawson M., 1990, AJ, 100, 1091
Press W. H., Flannery B. P., Teukolsky S. A., Vetterling W. T., 1986, Numerical Recipes. Cambridge Univ. Press, Cambridge
Richardson M. B., 1972, J. Opt. Soc. Am., 62, 55
Rix H. W., White S. D. M., 1992, MNRAS, 254, 389
Rix H. W., 1995, Kennicutt R. C. Jr., Braun R., Walterbos R. A. M., 1995, ApJ, 438, 155
Rix H. W., de Zeeuw T., Cretton N., van der Marel R. P., Carollo M., 1997, ApJ, 488, 702
Roberts M. S., Hogg D. E., Bregman J. N., Forman W. R., Jones C. R., 1991, ApJS, 75, 751
Ryden B., 1992, ApJ, 386, 42
Sandage A., Bedke J., 1994, The Carnegie Atlas of Galaxies. Carnegie Institution, Flintridge Foundation, Washington (CAG)
Sandage A., Tammann G. A., 1981, A Revised Shapley–Ames Catalog of Bright Galaxies. Carnegie Institution, Washington (RSA)
Sargent W. L. W., Schechter P. L., Boksenberg A., Shortridge K., 1977, ApJ, 212, 326
Satoh C., 1980, PASJ, 32, 41
Scorza C., Bender R., 1990, A&A, 235, 49
Simien F., Michard R., 1984, in Nieto J.-L., ed., New Aspects of Galaxy Photometry. Springer, Berlin, p. 345
Tohline J. E., Osterbrock D. E., 1976, ApJ, 210, L117
van der Marel R. P., 1991, MNRAS, 253, 710
van der Marel R.P., Cinzano P., 1992, in Busarello G., Capaccioli M., Longo G., eds, Morphological and Physical Classification of Galaxies. kluwer, Dordrecht, p. 437
van der Marel R. P., Franx M., 1993, ApJ, 407, 525
van der Marel R. P., Binney J. J., Davies R. L., 1990, MNRAS, 245, 582
van der Marel R. P., Rix H. W., Carter D., Franx M., White S. D. M., de Zeeuw P. T., 1994, MNRAS, 268, 521
White R. L., 1994, in Crabtree D. R., Hanisch R. J., Barnes J., eds, ASP Conf. Ser. Vol. 61, Astronomical Data Analysis Software and Systems III. Astron. Soc. Pac., San Francisco, p. 292

APPENDIX A: DATA TABLES

The stellar and ionized-gas heliocentric velocities and velocity dispersions measured along the major axis of NGC 4036 are given in Tables A1 and A2 respectively.

Table A1. Stellar kinematics along the major axis of NGC 4036.

r [″] (1)	V [km s^{-1}] (2)	δV [km s^{-1}] (3)	σ [km s^{-1}] (4)	$\delta\sigma$ [km s^{-1}] (5)
−27.9	1661	23	119	28
−21.0	1630	19	76	35
−17.9	1641	18	90	30
−15.5	1603	22	151	24
−13.5	1631	27	139	28
−12.0	1614	21	105	29
−10.9	1633	35	197	25
−9.9	1570	23	118	29
−9.1	1592	27	160	26
−8.4	1551	22	168	22
−7.8	1565	19	168	21
−7.1	1569	23	173	23
−6.4	1576	24	198	21
−5.8	1556	16	168	19
−5.1	1546	19	183	20
−4.4	1560	28	205	22
−3.8	1498	17	203	17
−3.1	1511	19	197	19
−2.5	1504	14	201	16
−1.8	1489	11	181	15
−1.1	1468	10	191	14
−0.5	1451	11	195	14
0.2	1407	10	209	13
0.8	1380	9	203	13
1.5	1363	11	185	15
2.1	1345	10	178	14
2.8	1330	12	189	16
3.5	1328	13	181	16
4.1	1302	16	191	18
4.8	1307	14	185	17
5.4	1304	14	144	20
6.1	1290	21	195	20
6.8	1290	19	170	21
7.4	1268	19	175	20
8.7	1299	34	207	25
9.4	1241	34	198	25
10.2	1266	17	110	26
11.2	1199	46	204	30
12.4	1186	28	141	28
13.7	1225	22	98	32
15.2	1239	24	140	26
17.0	1172	22	104	30
19.0	1193	23	131	26
21.1	1202	18	36	68
23.7	1155	26	176	24
29.1	1160	19	80	34

Table A2. Ionized-gas kinematics along the major axis of NGC 4036.

r [″] (1)	V [km s^{-1}] (2)	δV [km s^{-1}] (3)	σ [km s^{-1}] (4)	$\delta\sigma_+$ [km s^{-1}] (5)	$\delta\sigma_-$ [km s^{-1}] (6)
−25.4	1731	51	37	62	37
−20.8	1635	36	83	63	83
−15.8	1659	35	65	59	65
−14.2	1748	39	53	64	53
−12.5	1770	19	0	0	0
−10.9	1774	20	48	27	48
−9.2	1631	28	71	49	71
−7.8	1588	35	28	61	28
−7.1	1530	41	113	67	113
−6.4	1586	40	82	69	82
−5.8	1548	25	15	55	15
−5.1	1524	12	0	18	0
−4.5	1524	13	53	24	47
−3.8	1531	10	108	18	20
−3.1	1516	7	117	13	13
−2.5	1502	6	159	8	8
−1.8	1474	5	188	6	6
−1.2	1428	6	185	8	8
−0.5	1448	8	158	11	11
0.2	1466	8	167	12	12
0.8	1418	6	189	8	8
1.5	1358	6	211	7	7
2.1	1333	6	219	8	8
2.8	1330	6	191	8	8
3.5	1338	7	169	10	10
4.1	1330	10	142	15	16
4.8	1329	19	166	27	28
5.4	1282	24	141	36	39
6.1	1306	20	41	37	41
6.8	1257	23	142	34	36
7.4	1247	34	102	57	97
8.1	1242	22	0	38	0
8.7	1232	35	153	50	55
9.4	1183	24	0	27	0
10.1	1246	31	103	53	75
11.6	1200	39	77	67	77
13.2	1239	31	100	53	85
14.9	1254	33	43	55	43
19.1	1211	25	17	53	17
22.8	1256	31	29	55	29
28.0	1157	37	0	66	0

This paper has been typeset from a TEX/LATEX file prepared by the author.